scientific reports

Check for updates

OPEN

Contrast subgraphs catch patterns of altered functional connectivity in autism spectrum disorder

Tommaso Lanciano[1,2], Giovanni Petri[2,4], Tommaso Gili[3]✉ & Francesco Bonchi[2]

Despite the breakthrough achievements in understanding structural and functional alterations of brain connectivity in autism spectrum disorder (ASD), the exact nature and type of such alterations are not yet clear due to conflicting reports of hyper-connectivity, hypo-connectivity, and—in some cases—combinations of both. In this work, we bring order to the debate using a network comparison technique to capture mesoscopic-scale differential patterns of functional connectedness. In particular, we leverage recent algorithmic advances in extracting contrast subgraphs to identify maximally different mesoscopic connectivity structures between two sets of networks from typically developed individuals and ASD subjects across different developmental stages. A significantly larger connectivity among occipital cortex regions and between the left precuneus and the superior parietal gyrus was found in ASD subjects. At the same time, reduced connectivity characterized the superior frontal gyrus and the temporal lobe regions. More importantly, our results reconcile within a single framework multiple previous separate observations about functional connectivity alterations in ASD.

Keywords Functional brain networks, Contrast subgraphs, Autism spectrum disorder, Network neuroscience, Functional connectivity

Autism spectrum disorder (ASD) is associated with disrupted or altered brain connectivity[1] at both structural[2] and functional[3] levels. Deviations of the functional connections among brain regions from the normal pattern of connectivity are associated with several functional impairments[4,5]. Specifically, alterations of the functional connectivity strength among brain regions support a variety of social[6,7], cognitive[8,9], and sensorimotor[10,11] functions in ASD subjects. Indeed, experimental evidence exists of a correlation between functional connectivity perturbations and ASD symptom severity[12] and adaptive behaviour[13]. Despite the incredible results achieved in understanding both structural and functional connectivity alterations in ASD, the exact nature and type of such alterations are not completely clear due to conflicting reports of hyper-connectivity[14,15], hypo-connectivity[16], and—in some cases—combinations of both[17].

In this context, identifying specific neuroimaging-based biomarkers for ASD, especially ones that could be related to symptoms severity, is still a challenging task, usually requiring large-scale datasets and analyses[18,19]. The reason is that, in addition to the issues described above, to be effective such biomarkers have not only to reach statistical significance but also to be stable across multiple datasets, experimental designs and subjects[20]. Similarly to other alterations of functional connectivity[21], existing methods rely either on the identification of network features specific to the ASD spectrum[22] or on opaque neural network techniques[23,24].

In this work, we adopt a mesoscopic approach to the debate about hyper– vs hypo–connectivity in ASD, leveraging recent advances in network comparison techniques[25]. We thus develop a pipeline for the extraction of group-level *contrast subgraphs*, which are maximally different, in terms of connectivity level, between the brain networks of typically developed (TD) individuals and ASD subjects. We equip our approach with simultaneous mining of different subgraphs exhibiting this property, making it able to provide a variety of findings at the same time. For example, we show here that, under these goggles, it is possible to reframe previous results on functional network architectures in ASD in terms of a complex interplay between hyper- and hypo-connectivity, which evolves across age and relates deeply to individual differences. In addition to the group-level discrimination, the information obtained from contrast subgraphs can be used to build individual-level networks, which can then be studied in relation to individual phenotypical properties, as, for example, cognitive and social performances.

[1]DIAG, Sapienza University, Via Ariosto 25, 00185 Rome, Italy. [2]CENTAI Institute, Corso Inghilterra 3, 10138 Turin, Italy. [3]Networks Unit, IMT School for Advanced Studies Lucca, Piazza San Francesco 19, 55100 Lucca, Italy. [4] NP Lab, Network Science Institute, Northeastern University London, London, United Kingdom. ✉email: tommaso.gili@imtlucca.it

Results

To identify discriminating structures in functional networks of neurotypical and ASD subjects, we adopt the ABIDE dataset of resting-state functional networks[11]. In particular, we use resting-state fMRI data from 57 males with ASD (15 children, 42 adolescents) and 80 typically developed (TD) (17 children, 63 adolescents) males (see Supplementary Information for further details). For any participant, we compute standard functional connectivity matrices from the preprocessed timeseries using Pearson's correlation coefficient[30] (Fig. 1A). Each matrix is then sparsified using the SCOLA algorithm[26,27], to obtain an individual sparse weighted network (with densities typically $\rho < 0.1$ consistent with standard sparsification methods[31]).

Our aim is to detect multiple sets of regions of interest (ROIs) that, given a single cohort, simultaneously show hyper-connectivity in one group and hypo-connectivity in the other group. This can be achieved by appropriately building on recent methodology[25], which looks for the densest subset of edges between two groups to obtain a maximally discriminating subgraph.

Given two cohorts of individuals, for each group, we combine the group's functional networks in a single graph, dubbed *summary graph*: this step is crucial because it compresses in a single observation the common peculiarities of a set of networks. Next, we combine the two summary graphs in a *difference graph*, a new network whose edges have weights equal to the difference of the weights of the two summary graphs (Fig. 1B). Once the *difference graph* is computed, an optimization problem is defined on it[25], whose solution is the *contrast subgraph*, i.e., the set of ROIs that maximizes the difference in terms of density between the graphs of the two groups. In the Methods section, we provide further details on the technical implementation of the optimization.

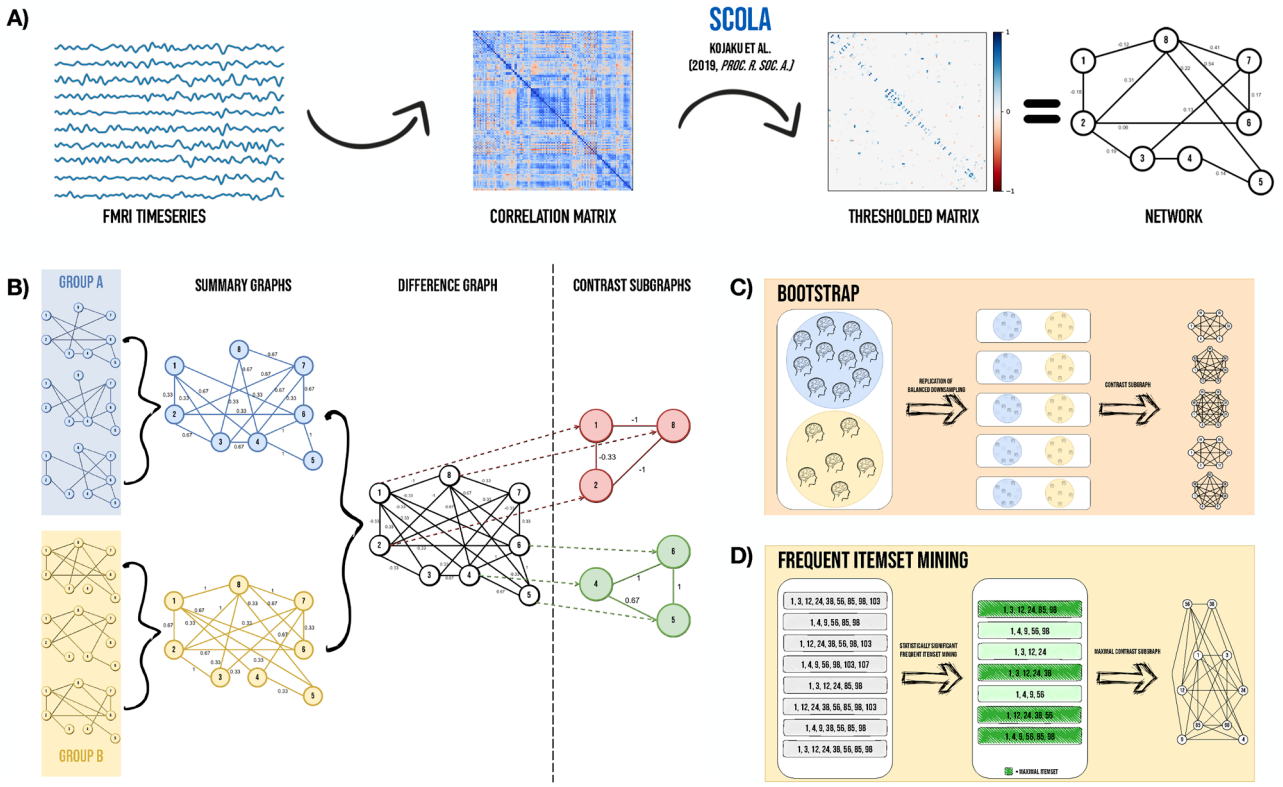

Fig. 1. Processing pipeline. (**A**) fMRI preprocessing: We use BOLD timeseries to construct functional connectivity (FC) matrices, which we then sparsify using state-of-art network filtering techniques[26,27] to obtain sparse functional networks. (**B**) Computation of the contrast subgraph[25]: Given the functional networks for two subject groups, the first step is to reduce both of them to their relative *summary graph*. Once both groups have been reduced, an optimisation problem is defined over the *difference graph*. Finally, we can solve and refine the optimisation problem with a local search approach. The final result is a set of nodes, dubbed *contrast subgraph*. In this instance, the two solutions make it clearer the approach followed: the set of nodes $\{1, 2, 8\}$ is sparsely connected in the Group *A*, while it shows a large number of connections in the graphs of Group *B*. The set of vertices $\{4, 5, 6\}$ shows the opposite pattern: density in the observations of Group *A* and sparsity in those of Group *B*. (**C**) Bootstrap of solutions: to compare unbalanced groups, we apply a down-sampling of the most populated group, such that it makes the groups balanced. For each resampled reduced dataset, we recompute the contrast subgraph as in (**B**), adopting as a value of α the one expressed by the proposal in[28]. (**D**) Alignment of bootstrap solutions: starting from the solutions obtained in the Bootstrap pipeline, we compute the statistically significant (overrepresented) maximal frequent itemsets[29], i.e. those that are not a subset of any other itemset. We compute the final solution as the union of these statistically significant maximal frequent itemsets (set of nodes) and the corresponding set of edges.

To improve the robustness of the solution and avoid limitations induced by class imbalances in the dataset, we iterate the detection of the contrast subgraphs by bootstrapping on equally-sized samples from the various populations (Fig. 1C). In this way, we obtain a family of contrast subgraphs rather than a single one. We then further select a *statistically significantly overrepresented* set of nodes from all these candidate contrast subgraphs, using techniques from Frequent Item-set Mining. This guarantees the robustness of the final contrast subgraph together with its statistical significance in discriminating between groups (Fig. 1D).

Contrast subgraphs classify subject group

Following the methods described above, we extract the two edge-sets that define the contrast subgraphs encoding the main network-level differences between the two groups. Since these edge-sets are determined at the group level, it is naturally possible to observe fluctuations in the individual-induced subgraphs –the graph obtained by projecting the subgraph of the individual functional connectivity on the edges induced by such dense sets of nodes. This leads to variable levels of hyper/hypo-connectivity, measured in terms of the weights' sum of edges in the induced subgraph across subjects.

Indeed, by considering these overall connectivity levels (as described in Methods and Fig. 1), we can obtain a simple rule to classify subjects in one of the two groups according to the separation boundary that separates subjects in terms of their induced graph density. While identifying this boundary is not the primary aim of the contrast subgraph extraction method, the differences in densities between groups (Fig. 2A) are clear. To confirm this and validate the goodness of our solution, we solve the classification task described above over any repetition of the bootstrap, running a linear SVM over the whole dataset to find a linear separation bound between the two groups, which can classify with large accuracy (children, 0.80 ± 0.06; adolescents, 0.68 ± 0.04).

Node-level description of contrast subgraphs

Below we report in the extended form our results for hyper- and hypo-connectivity patterns in ASD individuals (as compared to TD ones), separately for children and adolescents. All the reported regions and substructures have been statistically validated for the contrast generated by the two classes, according to the U-Test ($p < 0.05$). If not otherwise indicated, brain regions reported must be considered as bilaterally involved. Figure 2B shows the contrast subgraphs for the age groups (left, children; right, adolescents), highlighting the edges retained in

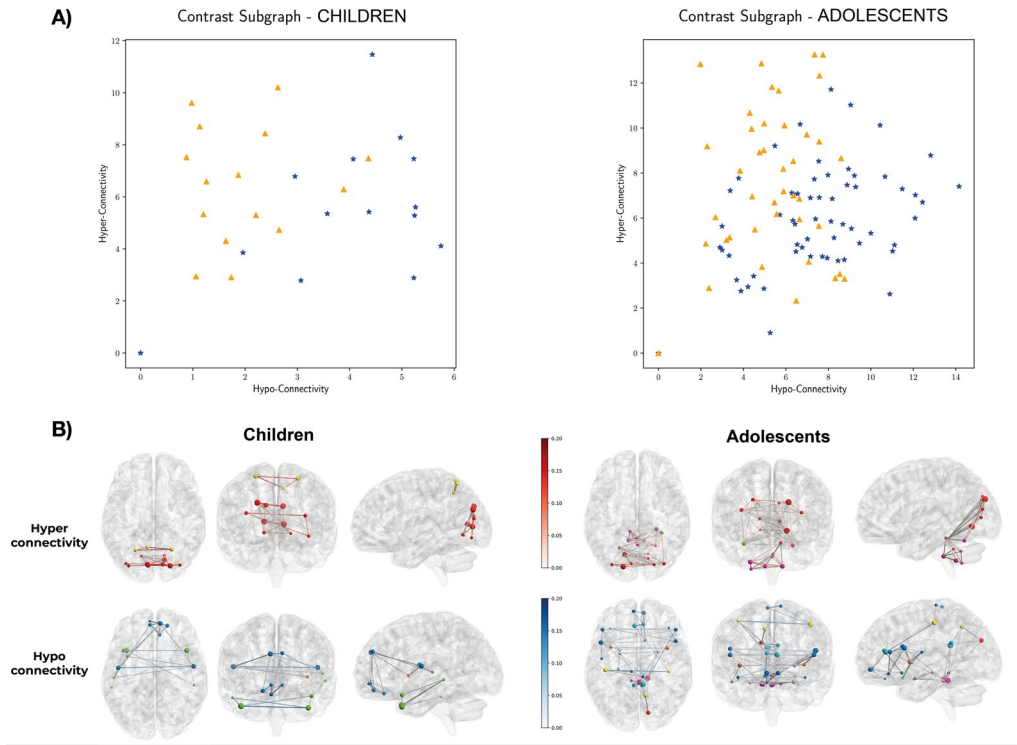

Fig. 2. (**A**) Level of hyper-connectivity and hypo-connectivity for Children(left) and Adolescents(right). Connectivity is expressed as the number of edges inside the contrast subgraph. We refer to hyper-connectivity for the solution denser for ASD (orange triangle) and sparser in TD (blue stars), and vice versa for hypo-connectivity. See main text for accuracy reports. (**B**) Visualization of the contrast subgraphs for the two age groups, children (left) and adolescents (right). Red (blue) edges represent edges present in the contrast subgraph for the ASD subjects (TD subjects). Nodes' color code refer to the different lobes they belong to: blue–frontal lobe; orange–insula; cyan–cingulate cortex; grey–deep grey matter; green– temporal lobe; red–occipital lobe; yellow–parietal lobe; magenta–cerebellum.

the contrast subgraphs that are hyper-(hypo-)expressed in ASD subjects as compared to TD ones (Fig. 2B top and bottom row, respectively).

Children. *Hypo-connectivity:* We find the subgraph mostly localized inside the Frontal Lobe. In particular, we find a central role of the Superior Frontal Gyrus (Medial), that shows, bilaterally, hypo-connectivity with two different sub-modules: (i) Orbital part of the Superior Frontal Gyrus, Medial Orbital part of the Superior Frontal Gyrus and Right Rectus; (ii) Rolandic Operculus, Left Insula and Left Superior Temporal Gyrus. Inside the Temporal Lobe, in particular between the Temporal Pole of the Superior and Middle Temporal Gyrus, and their connections with Right Inferior Temporal Gyrus and Left Middle Temporal Gyrus.

Children. *Hyper-connectivity:* We find localized structures: between Middle Occipital Gyrus and Left Inferior Occipital Gyrus; between Calcarine, Cuneus, Lingual and Right Superior Occipital Gyrus; and between the Superior Parietal Gyrus and the Left Precuneus.

Adolescents. *Hypo-connectivity:* We find, in this case, a huge contrastive structure involving different patterns of disconnection that include: (i) Inferior Frontal Gyrus (Triangular, Opercular and Orbital parts), the Insula, Left Putamen, Left Rolandic Operculus and the Temporal Pole of the Right Temporal Gyrus; (ii) Amygdala and Left Hyppocampus; (iii) Posterior Cingulate Gyrus, Right Cuneus and Right Precuneus; (iv) Vermis 3 and Left Cerebellum 3. Each submodule shows a significant disconnection from the cerebellar Vermis 1 and 2 and the Right Cerebellum 3. We also find a unique contrast subgraph composed of: the Postcentral and the Anterior Cingulate Gyrus, the Orbital Part of the Middle Frontal Gyrus, the Right Olfactory cortex, the Paracentral Lobule and the Orbital Part of the Middle Frontal Gyrus.

Adolescents. *Hyper-connectivity:* The Contrast subgraphs are localized in the Occipital Lobe (Superior and Middle Occipital Gyrus, Lingual, Calcarine and Left Cuneus) with connections with the Right Fusiform and the Left Cerebellum 6. We also find nodes within and between Cerebellum (Left 3, Right 8, 9, Right 10) and Vermis (9 and 10).

Lobes integration mesoscopic differences across age-groups

To summarise the information and to understand how the large-scale integration patterns differ across conditions, we coarse-grain the individual induced subgraphs from nodes to brain lobes. We then select the edges expressed in a significantly stronger way in ASD than in TD subjects for each age group, which we denote as *hyper-expressed*, and those that are instead weaker in adolescents versus children, which we denote as *hypo-expressed* (see 4.5) for details).

In Fig. 3 we show the adjacency matrices of the lobe-level induced graphs, divided by hyper- and hypo-expression for the four conditions. The first observation is that, at the mesoscopic level, both hyper- and hypo-expressed ASD-induced graphs show significant connectivity between occipital and cerebellar regions, which is instead absent in the case of TD subjects. More in detail, we also see that the amount of hypo- and hyper-expression is larger for ASD than for TD graphs between the occipital and temporal lobes and within the cerebellum. Together these observations suggest a nuanced reorganization of the ASD subjects' brains from childhood to adolescence than in TD subjects. In particular, we do not only observe increased or decreased connectivity, but we also find a combination of both effects simultaneously. We also find that lobes differ in the evolution of their self-interaction across age and condition (Fig. 4). In particular, for the cingulate lobe, deep grey Matter, and insula, we find a significant increase (linear regression, $p < 0.05$ on all coefficients) of lobe integration with age for TD subjects, which is instead absent in ASD individuals. The parietal and temporal lobes show conflicting trends: in the former, self-integration significantly increases for TD subjects and decreases for ASD subjects, while for the latter, the trends are reversed. Finally, we find that the cerebellum is progressively more integrated with age in both groups, but the increase of integration with age is significantly larger for ASD subjects. For the frontal and occipital lobes, we did not find any significant group-level effect with age for either ASD or TD subjects (see Table 1 for details). Overall, our analysis shows that, whereas TD subjects develop greater local integration within lobes as they grow, ASD subjects maintain a more distributed architecture, with the notable exceptions of the cerebellum and the temporal lobe.

Induced contrast subgraphs correlate with individual phenotypes

The contrast subgraphs discussed so far describe the salient features of each subject group and condition. However, inspired by the previous results, we wonder whether any differences observed at the lobe-level integration correlate with individual performance. We can investigate this by considering changes in individual architectures within the same group, for example, whether these sets can highlight individual phenotypical differences. To do this, we consider the induced contrast subgraphs at the individual level: given a cohort of subjects, once computed the contrast subgraph C^{g_1,g_2}, i.e., the set of nodes whose induced subgraph is denser in group g_1 and sparser in group g_2, we consider, for any individual *i* of the cohort, the subgraph $\mathcal{G}_i^{g_1,g_2}$ obtained by restricting the functional connectivity network of *i* to the edge-set induced by the node-set C^{g_1,g_2}. We then investigate whether simple graph metrics, i.e., lobe integration strength and lobe-lobe integration strength, correlate with the subjects' phenotypes as measured by standard performance scales[33,34]. In Fig. 5 we report the statistically significant ($p < 0.05$ Bonferroni corrected) relationships we obtain. We find that cerebellar and occipital lobe integrations are negatively correlated with standard intelligence scores (F/VIQ), and that the strength of the interaction between the occipital and temporal lobes in the lobe-level graphs associates with more severe social symptoms.

Discussion

Using contrast subgraph analysis, we elucidated atypical resting-state brain functional connectivity underlying the symptoms of ASD both in children and adolescents. Specifically, we analyzed a large rs-fMRI dataset from the ABIDE database to determine whether neurophysiological changes typical of the disease are associated with

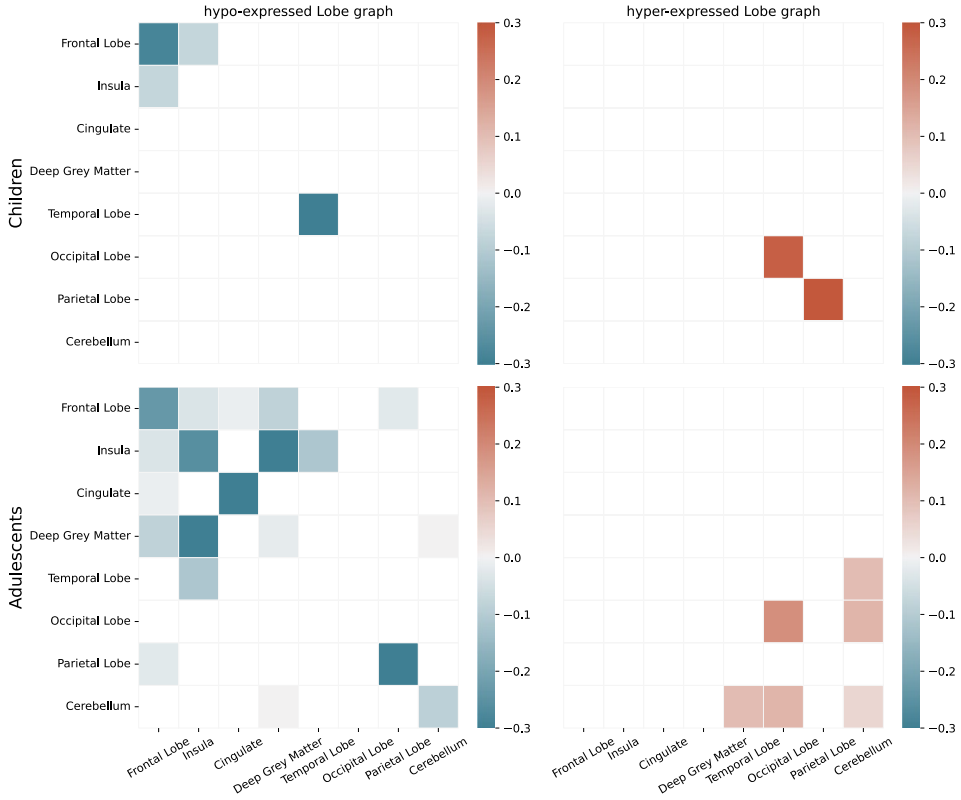

Fig. 3. Hyper and hypo-integration of lobes in ASD subjects vs TD subjects for the two age groups. We select either hypo- or hyper-expressed edges in the induced subgraphs corresponding to the various conditions and then coarse-grain the resulting networks to the lobe level to highlight the mesoscopic differences in the integration patterns across groups. Positive/negative values imply stronger edges within/between lobes (by coarse graining over the corresponding regions) in adolescents/children subjects. Overall, we find stronger interactions between occipital and temporal lobes in ASD for TD, larger differences within the cerebellar areas, and–finally–between the cerebellum and the occipital lobe.

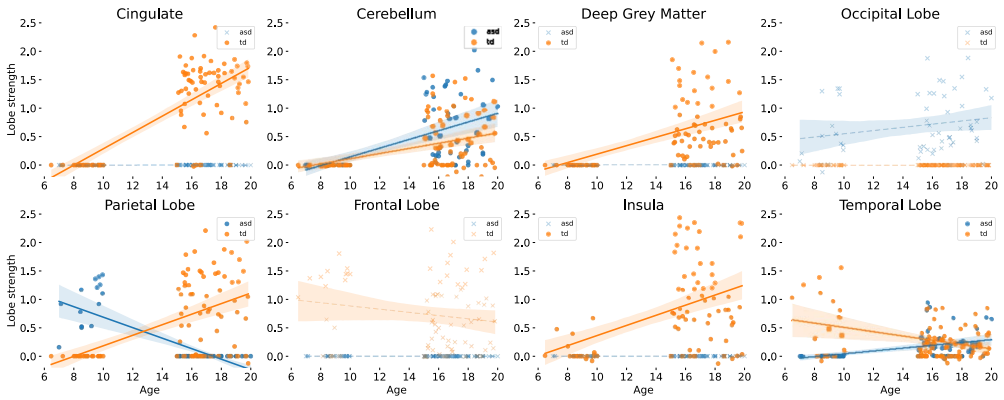

Fig. 4. Age dependence of lobe self-strength in induced lobe graphs. Full dots represent quantities for which the linear regression coefficients are significant ($p \leq 0.05$, full results in Table 1), while crosses show results for quantities for which we find no significant trend. For most lobes, we find a significant increase with the age of lobe-level self-strength for TD subjects. In contrast, ASD subjects only show significant increases in the temporal lobe and cerebellum.

cortico-cortical and cortico-subcortical dysfunctional connectivity in the brains of males with ASD. Our findings indicated that children of the ASD group exhibited a significantly larger number of functional connections among regions of the occipital cortex and between the left precuneus and the superior parietal gyrus. At the same time, reduced connectivity characterized the superior frontal gyrus as well as regions of the temporal lobe.

	ASD t	ASD p	TD t	TD p
Deep grey matter	–	–	3.764550	3.216810e-04
Parietal lobe	−8.629239	8.323787e-12	4.757780	8.823525e-06
Temporal lobe	3.496506	9.403944e-04	−3.765146	3.210339e-04
Cerebellum	5.598709	7.090777e-07	3.703659	3.948626e-04
Cingulate	–	–	9.437933	1.529787e-14
Frontal lobe	–	–	−0.526305	6.001697e-01
Insula	–	–	3.092880	2.750249e-03
Occipital lobe	1.441455	1.551258e-01	–	–

Table 1. Statistical results for Fig. 4. Missing values correspond to cases in which the regression was not possible because there were no links in the corresponding lobes.

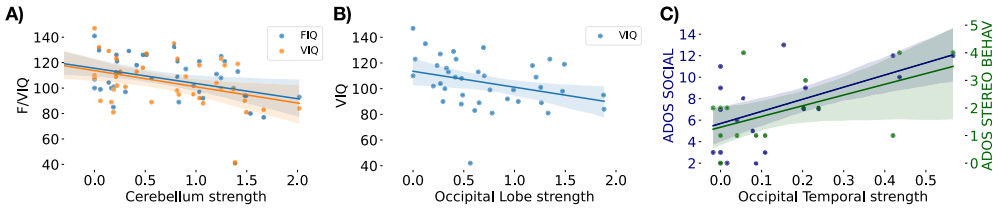

Fig. 5. Association between lobe strengths and lobe interactions with phenotypes in ASD adolescents. We report i) the significant ($p < 0.01, t > 2$) associations between cerebellar (**A**)) and occipital (**B**) lobe strength, respectively, with intelligence scores, FIQ and VIQ; and ii) the significant association of the interaction strength between occipital and temporal lobes (**C**) with social scores (ADOS Social and ADOS Stereo Behaviour)[32].

Conversely, adolescents of the ASD group showed hypo connectivity of Vermis 1, Vermis 2 and right III lobule of the cerebellum, while hyper-connectivity was found between regions of the occipital cortex and the left IV lobule of the cerebellum and the right fusiform, as well as among the left III, the right 8, 9 and 10 lobules of the cerebellum and Vermis 9 and 10.

The method proposed here captures both hyper-connectivity and hypo-connectivity across the whole brain, as opposed to common functional connectivity approaches that typically are only able to unveil only one direction of alteration or a subset of brain regions involved[3,35,36]. Our results recapitulate previous evidence that autism is characterized by atypical large-scale brain functional connectivity in both directions[37] within a single framework. Previous human and model neuroimaging studies reported a variety of functional architectures specific to ASD[16,38,39]. Most of them did not directly allow the simultaneous observation of under- and over-expressed connectivity of regions across the whole brain in ASD individuals, both at the regional and lobe level and of their evolution during development.

On the one hand, our results show that along with the development of the functional connectivity over-expression pattern in ASD subjects include regions of the occipital cortex both in children and in adolescents, as already observed in previous rs-fMRI studies[40,41]. According to the weak central coherence model[42,43], overstimulated and underselective visual processing areas may dominate high-order cognitive processes in autism. This can lead to the reduced ability in contextual information integration during the execution of complex perceptual and executive tasks[44] and can be related to the increased connectivity of visual cortices[45–47]. We also find increased connectivity between visual regions across hemispheres, suggesting enhanced perceptual processing, as observed in[48–50] together with the intact inter-hemispheric transfer of visual information.

On the other hand, we find differential hyper-connectivity in children and adolescents. Specifically, while the increased bilateral connectivity in children characterized regions belonging to the parietal cortex, adolescents were characterized by increased integration of the cerebellum. Hyper-connectivity found between superior parietal gyrus and precuneus might reflect altered patterns of signal fluctuations[51] in the interaction between the networks these regions originate from (fronto-parietal and default mode network). This, in turn, can impair cognitive processing. Increased coordination with nonessential regions may introduce low-level cross-talk and spoiling signal across primary network components[44]. These results, therefore, constitute a possible source of the widely observed decreased connectivity within the Default Mode Network[52–55], which may stem from the disturbing abnormal connectivity that one of its hubs (precuneus) has with different and unrelated regions (bilateral superior frontal gyrus).

Remarkably, atypical visual exploration of both social and nonsocial scenes is often reported in ASD subjects with less precise and longer saccades, potentially reflecting difficulties in eyes movement control[56], exerted by the cerebellar lobules VIII-X and uvula/nodulus (Vermis IX-X)[57,58]. The increased connectivity of the cerebellar lobules VIII-X and Vermis IX-X observed in our study might relate to the frequently reported reduction in gamma-aminobutyric acidergic (GABAergic) Purkinje cells in ASD[59,60]. These cerebellar neurons send inhibitory projections to the deep cerebellar nuclei (the output nuclei of the cerebellum) and the posterior lobe

of the Vermis. Loss of these neurons is thought to lead to disinhibition of the deep cerebellar nuclei and of the uvula/nodulus lobules[44,61], which could explain the observed increased cerebellar integration and consequent abnormal eyes movement control in ASD subjects[62].

Patterns of regional hypo-connectivity in ASD have been widely reported[63–67]. Accordingly, children showed reduced connectivity in frontal and temporal regions, and adolescent showed two heterogeneous patterns of hypo-connectivity: one involving cerebellar-subcortical, cuneo-cerebellar, fronto-cerebellar and fronto-parietal connectivity, the other involving anterior cingulate cortical connectivity with the parietal (postcentral gyrus) and frontal regions. The developmental trajectory of the disorder across age is firstly characterized by the increased complexity of the disconnection patterns. In fact, children show a clear disgregation of the functional fronto-temporal network, already associated with impaired working memory processes[68], language difficulties[69] and diminished preferential attention to social cues[70]. In contrast, adolescents show functional network disconnections organized in a mosaic of modules.

Fronto-temporal[71,72] and insular-limbic[73] dysconnectivity associated with emotion deficits, posterior cingulate-cuneus[74,75] underconnectivity that reflects a slow and delayed maturation of the Default Mode Network associated with social impairments and cerebellar disconnections[76,77] associated to a reduced social cognition, somatosensory and language skills have been separately reported in literature. Once the regions of interest were grouped in eight anatomical macroareas, we calculated, subject by subject, the average correlation within each one and tested the possible topology-phenotype covariance. We found that cerebellar and occipital cortices integration negatively correlated with standard measures of IQ (VIQ/FIQ) in ASD adolescents only, while no significant correlation was observed in children. Similarly, the increased connectivity of occipital and temporal areas was significantly associated with reduced social skills in ASD adolescents (ADOS Social, stereotypical behaviour scales). Besides the reduced sample size because of data homogeneity reasons, the absence of similar correlations in children may also suggest a complex role of developmental reorganization during the development of cognitive skills.

Finally, from a methodological perspective, it is important to highlight two features of our approach.

The first is its mesoscopic nature. This is grounded in the optimization involved in extracting contrast subgraphs. The framework acts locally at the level of the single edge contribution (i.e. the difference in weight between the same edge in the two groups), but obtains global solutions because the optimization is defined across the whole network. Conceptually, this is similar to what is done, for example, in network modularity[78]: in that case, however, the focus is on the modular density structure of a single network, rather than on the most discriminating subgraph between graphs representing two groups (or conditions). Crucially, and similarly to other mesoscopic observables, such as network modules[79–81] and topological cavities[82–86], the differences detected by contrast subgraphs pertain to the level of coordination among sets of nodes, rather than to the alteration of the integration patterns of specific nodes[87,88].

The second is the statistical robustness of the mesoscale subgraph detection. As opposed to canonical statistical methods for the network comparison at group level[89–91], here we proposed an approach composed of a preliminary process of edges decimation to retain the statistically significant connections (i.e. Scola[27]) in each network. Subsequently, a non-parametric scheme for the definition of the statistically significant sets of edges that maximize the difference between groups in terms of edge density is implemented. This guarantees the statistical robustness of the results without invoking any parametric approach for extracting topological properties that discriminate differences among different groups of networks.

Naturally, the proposed method also suffers from some limitations. First, and somewhat trivially, due to its intrinsic mesoscopic nature, it is less able to detect localized differences. It should be adopted in situations where mesoscopic changes rather than specific regional ones are hypothesized. Second, the method has a resolution parameter, α, that has a clear algorithmic interpretation, but that might be of difficult interpretation from a clinical point of view. However, combined with principled thresholding techniques, our bootstrapping approach can effectively buffer for this problem. Third, in the optimization, we considered a simple difference between the summary graphs with a penalty term that does not depend on the individual edges nor the statistics of the graphs under comparison. This could be improved by substituting the penalty with one obtained from a network-generating model, e.g. a weighted configuration model[92,93]. We also tested for robustness of results by increasing the sample size, without finding significant modifications (see Supplementary Information).

Finally, an additional possible limitation of this study is the gender imbalance in the cohort investigated. Although ASD is diagnosed more frequently in males, it is not considered a male trait. Nonetheless, the prevalence ratio in ASD diagnosis is about 4:1 in favour of men, and the underlying reasons for this difference are still debated. A possible cause for such mismatch may be found in the way ASD is diagnosed. It is reported that women present more subtle or internalized symptoms and a greater tendency to mask or camouflage their traits to fit in[94]. On the other hand, evidence from multiple types of genetic risk and multiple members of families affected by ASD supports a female protective effect model, in which females have a higher liability threshold for receiving a diagnosis of ASD[95]. Unfortunately, even if it is clear that autism is a lifelong neurodevelopmental condition with a heterogeneous presentation in all genders, multicentric neuroimaging data repositories, such as ABIDE and ABIDE II, suffer from such gender imbalance, and, consequentially, our results do.

Methods

Subjects

Resting-state fMRI data from 57 males with ASD (15 children, 42 adolescents) and 80 typically developed (TD) (17 children, 63 adolescents) males were acquired from the Preprocessed Connectomes Project[32]. The data had been obtained from ABIDE[11], and preprocessed using the Data Processing Assistant for Resting-State fMRI (DPARSF)[96]. Participants were excluded if mean framewise displacement (FD) during the resting-state fMRI scan was greater than 0.10 mm, and the percentage of data points exceeding 0.10 mm was greater than 5%.

Groups were matched for age, IQ and mean FD. ASD diagnoses were confirmed using ADOS[34] and/or the Autism Diagnostic Interview-Revised (ADI-R;[33]). Participant characteristics are described in Supplementary Info (Tables S1 and S2).

Ethics statement

The present study was carried out using rs-fMRI data from the Autism Imaging Data Exchange (ABIDE I). ABIDE is a consortium that provides previously collected rs-fMRI ASD and matched control data for data sharing in the scientific community[11,97]. The ABIDE datasets were collected at 17 different imaging sites. The Ethics Committee of each site approved the study protocol which was conducted in accordance with the Helsinki Declaration[98]. Prior to data contribution, sites are required to confirm that their local Institutional Review Board (IRB) or ethics committee have approved both the initial data collection and the retrospective sharing of a fully de-identified version of the datasets (i.e., after removal of the 18 protected health information identifiers including facial information from structural images as identified by the Health Insurance Portable and Accountability Act [HIPAA]). Written informed consent or assent was obtained from all participants in accordance with respective IRB.

fMRI acquisition and preprocessing

Information about scanner types and parameters can be found on the ABIDE website. We carried out the following DPARSF preprocessing steps: slice timing correction, motion correction, realignment using a six-parameter (rigid body) linear transformation with a two-pass procedure (registered to the first image and then registered to the mean of the images after the first realignment). Individual structural images (T1-weighted MPRAGE) were co-registered to the mean functional image after realignment using a 6 degrees-of-freedom linear transformation without re-sampling. The transformed structural images were segmented into grey matter (GM), white matter (WM) and cerebrospinal fluid (CSF)[99] and nuisance parameters were regressed out (including 24 motion parameters, WM and CSF signals, linear and quadratic trends, and the global signal)[100]. Temporal filtering (0.01 - 0.1 Hz) was performed on the time series.

The Diffeomorphic Anatomical Registration Through Exponentiated Lie algebra (DARTEL) tool[101] was used to compute transformations from individual native space to MNI space. We chose to use data that had the global signal regressed out, as this step has been shown to help mitigate differences across multiple sites[102]. Furthermore, it has been shown recently that global signal regression attenuates artifactual changes in BOLD signal that are introduced by head motion[103,104]. The time series of 116 regions of interest (ROIs) from the Automated Anatomical Labeling (AAL) atlas[105] were obtained. Additional details of the fMRI preprocessing steps can be found on the Preprocessed Connectomes Project website.

To standardize the length of all observations, we trimmed the time serieses to the 140 central records of each fMRI region signal.

For any participant, we computed standard functional connectivity matrices from the preprocessed timeseries using Pearson's correlation coefficient[30] (Fig. 1A). We then sparsified each matrix using recent network-theoretical methods (SCOLA[26,27]), to obtain the individual sparse weighted network (with densities typically $\rho < 0.1$ consistent with standard sparsification methods[31]). To run the SCOLA algorithm, we configured the parameters as follows: $L = 140$ to match the length of the available time series, and $\beta = 0.5$ as recommended by the authors. For the null model, we tested all the options proposed by the authors and selected the configuration model, as it consistently provided the best average BIC score.

Computation and robustness of contrast subgraphs

We make use of a dataset $\mathcal{D}$ of functional networks, where the i-th observation corresponds to the sparse weighted network of the i-th individual, each one defined over the same set of nodes V (i.e., the 116 regions of the AAL atlas). $\mathcal{D}$ can be divided into two cohorts $c = \{\text{children}, \text{adolescents}\}$, each one composed of individuals belonging two one of the groups $g = \{\text{TD}, \text{ASD}\}$. Starting from the preprocessed functional connectivity networks $\{\mathcal{G}\}$ for the two groups $\mathcal{A}$ and $\mathcal{B}$, we construct the *summary graphs* $G^{\mathcal{A}}$ and $G^{\mathcal{B}}$ by averaging over the group, and then search for the node subset S^* that maximizes the difference in terms of density between $G^{\mathcal{A}}_{|S^*}$, which is the subgraph of $G^{\mathcal{A}}$ restricted to S^*, and $G^{\mathcal{B}}_{|S^*}$, correspondingly the subgraph of $G^{\mathcal{B}}$ restricted to S^*. The *contrast subgraph* $G^{\mathcal{A}-\mathcal{B}}$ between groups $\mathcal{A}$ and $\mathcal{B}$ is the subgraph induced by the set of nodes $V_{\{\mathcal{A}-\mathcal{B}\}}$ such that the subgraphs of the original networks induced by $V_{\{\mathcal{A}-\mathcal{B}\}}$ has maximal density for group $\mathcal{A}$ with respect to group $\mathcal{B}$(Fig. 1B). In other words, our proposal aims to detect a set of regions of interest (ROIs) that simultaneously shows hyper-connectivity in one group and hypo-connectivity in the other group. This can be achieved by appropriately generalizing the methodology proposed by Lanciano et al.[25] to fit our purposes.

The pipeline just described has three main limitations that need to be taken into account:

1. Dependence of the contrast subgraph extraction on an accuracy parameter α(see Supporting information for formal definition): indeed, depending on the value of α, it is possible to exclude potential ROIs that are contrastive but not the most contrastive one;
2. Potential group imbalance in the dataset. Imbalances between the number of subjects in each class can affect the optimization results, biasing it toward one of the classes;
3. Design of the contrast subgraph model of[25] as an optimization problem whose output is a single solution; other subgraphs with an associated high level of contrast might be not detected in this way.

Therefore, starting from the algorithm provided in[25], we employ an enhance to the existing pipeline to efficiently address all these limitations.

To overcome the first issue, we relate our choice of the value of the parameter α to follow the proposal of[28]; in their work the authors address the existing problem of thresholding complete graphs generated from correlation matrices, providing a topological criterion that filter the weakest edges preserving the balance in the trade-off between network's efficiency (i.e., a measure that quantify how efficiently the information in a network can be exchanged) and number of edges. Since in the original proposal of[25] the parameter α is responsible to penalize the weakest edges in the network in such a way that the solution is contained in terms of size, we set it according to this criterion in order to guarantee the algorithm a search space that is represented by an efficient network.

In order to address the last two issues, we adopt the following strategy: as a first step, we generate multiple replications of the original dataset, each one composed by the less populated group of subjects and a subset of the second group of subjects of equal size of the first. In this way we are either able to overcome the second issue, since now all the available replications are balanced in terms of size, and pave the way to implement a strategy for the third: in fact, computing the contrast subgraph for each replication of the dataset, we obtain a set of candidate solutions. In order to ensure the representativeness of the obtained solutions, we test them via the Frequent Itemset Mining paradigm (Fig. 1D), retaining only those statistically significant.

Coarse-graining of subgraphs and statistical selection of reduced edges

Consider a graph G defined on the node set of regions V and with edges $E_G \subset V \times V$, and a set of lobes $L = \{L_i\}_i$, such that each lobe, $L_i \in L$ is a subset of V, $L_i \cap L_j = \emptyset$, and $\bigcup L = \bigcup_i L_i = V$. We coarse-grain individual graphs to lobe-level graphs by defining a new lob graph LG with node set L, and edges E_{LG}. Each edge $e = (u, v) \in E_G$ induces an edge in $e_{lg} = (L_i, L_j) \in E_{LG}$ such that $u \in L_i, v \in L_j$. The weight of such edge $\omega_{e_{lg}}$ is the sum of the weight of the edges e that link the corresponding lobes L_i, L_j, $\omega_{e_{lg}=(L_i,L_j)} = \sum_{e=(u,v)\in E_G | u\in L_i, v\in L_j} \omega_e$. Note that it is possible for u and v to belong to the same lobe $L_i = L_j$, and therefore the graph LG can have self-loops with arbitrary weights. In fact, in the main text we use extensively the node selfloop weight (named node self-strength or integration).

For the hypo- and hyper-expressed results reported in Fig. 3, we perform an additional step before coarse-graining from regions to lobes. In particular, for each link e in the constrast subgraph for ASD(TD) subjects we compute its average weight ω_e^{ASD} (ω_e^{TD}) in the two groups, we build the distribution over the edges of the differences $\Delta_e = \omega_e^{ASD} - \omega_e^{TD}$, and we keep only the edges in with the top 10% largest difference. We consider these edges hyper-expressed, and then coarse-grained the resulting graph to lobe level. For the hypo-expressed we perform the same procedure keeping the edges corresponding to the smallest 10% of differences.

Data availability

The anonymised data that support the findings of this study are available as open data through the ABIDE repository (https://fcon_1000.projects.nitrc.org/indi/abide/). The implementation of the algorithms is available by contacting the corresponding author.

Received: 5 March 2024; Accepted: 29 May 2025
Published online: 07 July 2025

References

1. Kana, R. K., Uddin, L. Q., Kenet, T., Chugani, D. & Müller, R.-A. Brain connectivity in autism. *Front. Hum. Neurosci.* **8**, 349 (2014).
2. Vissers, M. E., Cohen, M. X. & Geurts, H. M. Brain connectivity and high functioning autism: A promising path of research that needs refined models, methodological convergence, and stronger behavioral links. *Neurosci. Biobehav. Rev.* **36**, 604–625 (2012).
3. Hull, J. V. et al. Resting-state functional connectivity in autism spectrum disorders: A review. *Front. Psych.* **7**, 205 (2017).
4. Abrams, D. A. et al. Underconnectivity between voice-selective cortex and reward circuitry in children with autism. *Proc. Natl. Acad. Sci.* **110**, 12060–12065 (2013).
5. Supekar, K. et al. Brain hyperconnectivity in children with autism and its links to social deficits. *Cell Rep.* **5**, 738–747 (2013).
6. Gotts, S. J. et al. Fractionation of social brain circuits in autism spectrum disorders. *Brain* **135**, 2711–2725 (2012).
7. Abbott, A. E. et al. Patterns of atypical functional connectivity and behavioral links in autism differ between default, salience, and executive networks. *Cereb. Cortex* **26**, 4034–4045 (2016).
8. Nair, A. et al. Regional specificity of aberrant thalamocortical connectivity in autism. *Hum. Brain Mapp.* **36**, 4497–4511 (2015).
9. Farrant, K. & Uddin, L. Q. Atypical developmental of dorsal and ventral attention networks in autism. *Dev. Sci.* **19**, 550–563 (2016).
10. Rudie, J. D. et al. Altered functional and structural brain network organization in autism. *NeuroImage: Clin.* **2**, 79–94 (2013).
11. Di Martino, A. et al. The autism brain imaging data exchange: Towards a large-scale evaluation of the intrinsic brain architecture in autism. *Mol. Psychiatry* **19**, 659–667 (2014).
12. Fishman, I., Keown, C. L., Lincoln, A. J., Pineda, J. A. & Müller, R.-A. Atypical cross talk between mentalizing and mirror neuron networks in autism spectrum disorder. *JAMA Psychiat.* **71**, 751–760 (2014).
13. Plitt, M., Barnes, K. A., Wallace, G. L., Kenworthy, L. & Martin, A. Resting-state functional connectivity predicts longitudinal change in autistic traits and adaptive functioning in autism. *Proc. Natl. Acad. Sci.* **112**, E6699–E6706 (2015).
14. Chien, H.-Y., Lin, H.-Y., Lai, M.-C., Gau, S.S.-F. & Tseng, W.-Y.I. Hyperconnectivity of the right posterior temporo-parietal junction predicts social difficulties in boys with autism spectrum disorder. *Autism Res.* **8**, 427–441 (2015).
15. Ray, S. et al. Structural and functional connectivity of the human brain in autism spectrum disorders and attention-deficit/hyperactivity disorder: A rich club-organization study. *Hum. Brain Mapp.* **35**, 6032–6048 (2014).
16. Just, M. A., Keller, T. A., Malave, V. L., Kana, R. K. & Varma, S. Autism as a neural systems disorder: A theory of frontal-posterior underconnectivity. *Neurosci. Biobehav. Rev.* **36**, 1292–1313 (2012).
17. Coben, R., Mohammad-Rezazadeh, I. & Cannon, R. L. Using quantitative and analytic EEG methods in the understanding of connectivity in autism spectrum disorders: A theory of mixed over-and under-connectivity. *Front. Hum. Neurosci.* **8**, 45 (2014).
18. Abraham, A. et al. Deriving reproducible biomarkers from multi-site resting-state data: An autism-based example. *Neuroimage* **147**, 736–745 (2017).

19. Doyle-Thomas, K. A. et al. Atypical functional brain connectivity during rest in autism spectrum disorders. *Ann. Neurol.* **77**, 866–876 (2015).
20. Mueller, S. et al. Convergent findings of altered functional and structural brain connectivity in individuals with high functioning autism: a multimodal mri study. *PLoS ONE* **8**, e67329 (2013).
21. Gheiratmand, M. et al. Learning stable and predictive network-based patterns of schizophrenia and its clinical symptoms. *NPJ Schizophr.* **3**, 1–12 (2017).
22. Yerys, B. E. et al. Globally weaker and topologically different: Resting-state connectivity in youth with autism. *Mol. Autism* **8**, 1–11 (2017).
23. Sherkatghanad, Z. et al. Automated detection of autism spectrum disorder using a convolutional neural network. *Front. Neurosci.* **13**, 1325 (2019).
24. Aghdam, M. A., Sharifi, A. & Pedram, M. M. Combination of rs-fMRI and sMRI data to discriminate autism spectrum disorders in young children using deep belief network. *J. Digit. Imaging* **31**, 895–903 (2018).
25. Lanciano, T., Bonchi, F. & Gionis, A. Explainable classification of brain networks via contrast subgraphs. In *Proceedings of the 26th ACM SIGKDD International Conference on Knowledge Discovery & Data Mining*, KDD '20, 3308–3318, https://doi.org/10.1145/3394486.3403383 (Association for Computing Machinery, New York, NY, USA, 2020).
26. Masuda, N., Kojaku, S. & Sano, Y. Configuration model for correlation matrices preserving the node strength. *Phys. Rev. E* **98**, 012312 (2018).
27. Kojaku, S. & Masuda, N. Constructing networks by filtering correlation matrices: A null model approach. *Proc. Royal Soc. A* **475**, 20190578 (2019).
28. De Vico Fallani, F., Latora, V. & Chavez, M. A topological criterion for filtering information in complex brain networks. *PLoS Comput. Biol.* **13**, 1–18. https://doi.org/10.1371/journal.pcbi.1005305 (2017).
29. Kirsch, A. et al. An efficient rigorous approach for identifying statistically significant frequent itemsets. *J. ACM.* https://doi.org/10.1145/2220357.2220359 (2012).
30. Bassett, D. S. & Sporns, O. Network neuroscience. *Nat. Neurosci.* **20**, 353–364 (2017).
31. Hermundstad, A. M. et al. Structural foundations of resting-state and task-based functional connectivity in the human brain. *Proc. Natl. Acad. Sci.* **110**, 6169–6174 (2013).
32. Craddock, C. et al. The neuro bureau preprocessing initiative: Open sharing of preprocessed neuroimaging data and derivatives. *Front. Neuroinf.* **7**, 5 (2013).
33. Lord, C., Rutter, M. & Le Couteur, A. Autism diagnostic interview-revised: A revised version of a diagnostic interview for caregivers of individuals with possible pervasive developmental disorders. *J. Autism Dev. Disord.* **24**, 659–685 (1994).
34. Lord, C. et al. 2-year-old boy who has been diagnosed with autism. *J. Autism Dev. Disord.* **30**, 205–223. https://doi.org/10.1023/a:1005592401947 (2000).
35. Kana, R., Uddin, L., Kenet, T., Chugani, D. & Müller, R.-A. Brain connectivity in autism. *Front. Hum. Neurosci.* **8**, 349 (2014).
36. King, J. B. et al. Generalizability and reproducibility of functional connectivity in autism. *Mol. Autism* **10**, 27 (2019).
37. Uhlhaas, P. J. & Singer, W. Neuronal dynamics and neuropsychiatric disorders: Toward a translational paradigm for dysfunctional large-scale networks. *Neuron* **75**, 963–980 (2012).
38. Anderson, J. S. et al. Functional connectivity magnetic resonance imaging classification of autism. *Brain* **134**, 3742–3754 (2012).
39. Yahata, N. et al. A small number of abnormal brain connections predicts adult autism spectrum disorder. *Nat. Commun.* **7**, 11254 (2016).
40. Keown, C. L. et al. Local functional overconnectivity in posterior brain regions is associated with symptom severity in autism spectrum disorders. *Cell Rep.* **5**, 567–572 (2013).
41. Nair, S. et al. Local resting state functional connectivity in autism: Site and cohort variability and the effect of eye status. *Brain Imaging Behav.* **12**, 168–179 (2018).
42. Frith, U. *Autism: Explaining the enigma* (Blackwell Publishing, Oxford, 2003).
43. Happé, F. & Frith, U. The weak coherence account: Detail-focused cognitive style in autism spectrum disorders. *J. Autism Dev. Disord.* **36**, 5–25 (2006).
44. Belmonte, M. K. et al. Autism and abnormal development of brain connectivity. *J. Neurosci.* **24**, 9228–9231 (2004).
45. Groen, W. et al. Semantic, factual, and social language comprehension in adolescents with autism: An fmri study. *Cereb. Cortex* **20**, 1937–1945 (2010).
46. Shen, M. D. et al. Atypical lexicosemantic function of extrastriate cortex in autism spectrum disorder: Evidence from functional and effective connectivity. *Neuroimage* **62**, 1780–1791 (2012).
47. Jao Keehn, R. J. et al. Impaired downregulation of visual cortex during auditory processing is associated with autism symptomatology in children and adolescents with autism spectrum disorder. *Autism Res.* **10**, 130–143 (2017).
48. Barbeau, E. B. et al. A greater involvement of posterior brain areas in interhemispheric transfer in autism: fMRI, DWI and behavioral evidences. *NeuroImage: Clin.* **8**, 267–280 (2015).
49. Clawson, A., Clayson, P. E., South, M., Bigler, E. D. & Larson, M. J. An electrophysiological investigation of interhemispheric transfer time in children and adolescents with high-functioning autism spectrum disorders. *J. Autism Dev. Disord.* **45**, 363–375 (2015).
50. Jao Keehn, R. J. et al. Atypical local and distal patterns of occipito-frontal functional connectivity are related to symptom severity in autism. *Cereb. Cortex* **29**, 3319–3330 (2019).
51. Uddin, L. Q. et al. Salience network-based classification and prediction of symptom severity in children with autism. *JAMA Psychiat.* **70**, 869–879 (2013).
52. Lynch, C. J. et al. Default mode network in childhood autism: Posteromedial cortex heterogeneity and relationship with social deficits. *Biol. Psychiat.* **74**, 212–219 (2013).
53. Washington, S. D. et al. Dysmaturation of the default mode network in autism. *Hum. Brain Mapp.* **35**, 1284–1296 (2014).
54. Padmanabhan, A., Lynch, C. J., Schaer, M. & Menon, V. The default mode network in autism. *Biol. Psychiatry: Cognit. Neurosci. Neuroimaging* **2**, 476–486 (2017).
55. Kotila, A. et al. Atypical inter-network deactivation associated with the posterior default-mode network in autism spectrum disorder. *Autism Res.* **14**, 248–264 (2021).
56. Kovarski, K., Siwiaszczyk, M., Malvy, J., Batty, M. & Latinus, M. Faster eye movements in children with autism spectrum disorder. *Autism Res.* **12**, 212–224 (2019).
57. Vahedi, K., Rivaud, S., Amarenco, P. & Pierrot-Deseilligny, C. Horizontal eye movement disorders after posterior vermis infarctions. *J. Neurol., Neurosurg. Psychiatry* **58**, 91–94 (1995).
58. Stoodley, C. J. & Schmahmann, J. D. Evidence for topographic organization in the cerebellum of motor control versus cognitive and affective processing. *cortex* **46**, 831–844 (2010).
59. Bailey, A. et al. A clinicopathological study of autism. *Brain: J. Neurol.* **121**, 889–905 (1998).
60. Rubenstein, J. & Merzenich, M. M. Model of autism: Increased ratio of excitation/inhibition in key neural systems. *Genes. Brain Behav.* **2**, 255–267 (2003).
61. Cerliani, L. et al. Increased functional connectivity between subcortical and cortical resting-state networks in autism spectrum disorder. *JAMA Psychiat.* **72**, 767–777 (2015).
62. Trimarco, E., Mirino, P. & Caligiore, D. Cortico-cerebellar hyper-connections and reduced purkinje cells behind abnormal eyeblink conditioning in a computational model of autism spectrum disorder. *Front. Syst. Neurosci.* **15**, 666649 (2021).

63. Moseley, R. et al. Whole-brain functional hypoconnectivity as an endophenotype of autism in adolescents. *Neuroimage: Clin.* **9**, 140–152 (2015).
64. Roy, D. & Uddin, L. Q. Atypical core-periphery brain dynamics in autism. *Netw. Neurosci.* **5**, 295–321 (2021).
65. Cheng, W., Rolls, E. T., Gu, H., Zhang, J. & Feng, J. Autism: Reduced connectivity between cortical areas involved in face expression, theory of mind, and the sense of self. *Brain* **138**, 1382–1393 (2015).
66. Anderson, J. S. et al. Decreased interhemispheric functional connectivity in autism. *Cereb. Cortex* **21**, 1134–1146 (2011).
67. Nomi, J. S. & Uddin, L. Q. Developmental changes in large-scale network connectivity in autism. *NeuroImage: Clin.* **7**, 732–741 (2015).
68. Urbain, C. et al. Desynchronization of fronto-temporal networks during working memory processing in autism. *Hum. Brain Mapp.* **37**, 153–164 (2016).
69. Verly, M. et al. Structural and functional underconnectivity as a negative predictor for language in autism. *Hum. Brain Mapp.* **35**, 3602–3615 (2014).
70. Sperdin, H. F. et al. Early alterations of social brain networks in young children with autism. *Elife* **7**, e31670 (2018).
71. Alaerts, K. et al. Underconnectivity of the superior temporal sulcus predicts emotion recognition deficits in autism. *Soc. Cognit. Affect. Neurosci.* **9**, 1589–1600 (2014).
72. Malaia, E. A., Ahn, S. & Rubchinsky, L. L. Dysregulation of temporal dynamics of synchronous neural activity in adolescents on autism spectrum. *Autism Res.* **13**, 24–31 (2020).
73. Ebisch, S. J. et al. Altered intrinsic functional connectivity of anterior and posterior insula regions in high-functioning participants with autism spectrum disorder. *Hum. Brain Mapp.* **32**, 1013–1028 (2011).
74. Nair, A., Jolliffe, M., Lograsso, Y. S. S. & Bearden, C. E. A review of default mode network connectivity and its association with social cognition in adolescents with autism spectrum disorder and early-onset psychosis. *Front. Psych.* **11**, 614 (2020).
75. Bathelt, J. & Geurts, H. M. Difference in default mode network subsystems in autism across childhood and adolescence. *Autism* **25**, 556–565 (2021).
76. Long, Z., Duan, X., Mantini, D. & Chen, H. Alteration of functional connectivity in autism spectrum disorder: Effect of age and anatomical distance. *Sci. Rep.* **6**, 1–8 (2016).
77. Van Overwalle, F. et al. Consensus paper: Cerebellum and social cognition. *The Cereb.* **19**, 833–868 (2020).
78. Brandes, U. et al. On modularity clustering. *IEEE Trans. Knowl. Data Eng.* **20**, 172–188 (2008).
79. Sporns, O. & Betzel, R. F. Modular brain networks. *Annu. Rev. Psychol.* **67**, 613–640 (2016).
80. Esfahlani, F. Z. et al. Modularity maximization as a flexible and generic framework for brain network exploratory analysis. *Neuroimage* **244**, 118607 (2021).
81. Sigar, P., Uddin, L. Q. & Roy, D. Altered global modular organization of intrinsic functional connectivity in autism arises from atypical node-level processing. *bioRxiv* (2022).
82. Petri, G. et al. Homological scaffolds of brain functional networks. *J. R. Soc. Interface* **11**, 20140873 (2014).
83. Ibáñez-Marcelo, E., Campioni, L., Phinyomark, A., Petri, G. & Santarcangelo, E. L. Topology highlights mesoscopic functional equivalence between imagery and perception: The case of hypnotizability. *Neuroimage* **200**, 437–449 (2019).
84. Lee, H., Kang, H., Chung, M. K., Kim, B.-N. & Lee, D. S. Persistent brain network homology from the perspective of dendrogram. *IEEE Trans. Med. Imaging* **31**, 2267–2277 (2012).
85. Chung, M. K., Lee, H., DiChristofano, A., Ombao, H. & Solo, V. Exact topological inference of the resting-state brain networks in twins. *Netw. Neurosci.* **3**, 674–694 (2019).
86. Sizemore, A. E. et al. Cliques and cavities in the human connectome. *J. Comput. Neurosci.* **44**, 115–145 (2018).
87. Lin, P. et al. Global and local brain network reorganization in attention-deficit/hyperactivity disorder. *Brain Imaging Behav.* **8**, 558–569 (2014).
88. Gallos, L. K., Makse, H. A. & Sigman, M. A small world of weak ties provides optimal global integration of self-similar modules in functional brain networks. *Proc. Natl. Acad. Sci.* **109**, 2825–2830 (2012).
89. Zalesky, A., Fornito, A. & Bullmore, E. T. Network-based statistic: Identifying differences in brain networks. *Neuroimage* **53**, 1197–1207 (2010).
90. Ginestet, C. E. & Simmons, A. Statistical parametric network analysis of functional connectivity dynamics during a working memory task. *Neuroimage* **55**, 688–704 (2011).
91. Bahrami, M., Laurienti, P. J. & Simpson, S. L. Analysis of brain subnetworks within the context of their whole-brain networks. *Hum. Brain Mapp.* **40**, 5123–5141 (2019).
92. Garlaschelli, D. & Loffredo, M. I. Generalized bose-fermi statistics and structural correlations in weighted networks. *Phys. Rev. Lett.* **102**, 038701 (2009).
93. Voitalov, I., Van Der Hoorn, P., Kitsak, M., Papadopoulos, F. & Krioukov, D. Weighted hypersoft configuration model. *Phys. Rev. Res.* **2**, 043157 (2020).
94. Hull, L., Petrides, K. & Mandy, W. The female autism phenotype and camouflaging: A narrative review. *Rev. J. Autism Dev. Disord.* **7**, 306–317 (2020).
95. Wigdor, E. M. *et al.* The female protective effect against autism spectrum disorder. *Cell Genom.***2**(6), (2022).
96. Yan, C. DPARSF: A MATLAB toolbox for pipeline data analysis of resting-state fMRI. *Front. Syst. Neuroscie.* https://doi.org/10.3389/fnsys.2010.00013 (2010).
97. Di Martino, A. et al. Enhancing studies of the connectome in autism using the autism brain imaging data exchange ii. *Sci. Data* **4**, 1–15 (2017).
98. Association, W. M. et al. Ethical principles for medical research involving human subjects. *Eur. J. Emerg. Med.: Off. J. Eur. Soc. Emerg. Med.* **8**, 221–223 (2001).
99. Ashburner, J. & Friston, K. J. Unified segmentation. *Neuroimage* **26**, 839–851 (2005).
100. Satterthwaite, T. D. et al. An improved framework for confound regression and filtering for control of motion artifact in the preprocessing of resting-state functional connectivity data. *Neuroimage* **64**, 240–256 (2013).
101. Ashburner, J. A fast diffeomorphic image registration algorithm. *Neuroimage* **38**, 95–113 (2007).
102. Power, J. D. et al. Methods to detect, characterize, and remove motion artifact in resting state fMRI. *Neuroimage* **84**, 320–341 (2014).
103. Ciric, R. et al. Benchmarking of participant-level confound regression strategies for the control of motion artifact in studies of functional connectivity. *Neuroimage* **154**, 174–187 (2017).
104. Power, J. D., Plitt, M., Laumann, T. O. & Martin, A. Sources and implications of whole-brain fMRI signals in humans. *Neuroimage* **146**, 609–625 (2017).
105. Tzourio-Mazoyer, N. et al. Automated anatomical labeling of activations in SPM using a macroscopic anatomical parcellation of the MNI MRI single-subject brain. *Neuroimage* **15**, 273–289 (2002).

Acknowledgements

Tommaso Gili thankfully acknowledges financial support by the European Union Horizon 2020 Program under the INFRAIA-01-2018-2019 Integrating Activities for Advanced Communities, Grant Agreement n. 871042, SoBigData++: European Integrated Infrastructure for Social Mining and Big Data Analytics. Giovanni Petri acknowledges support from the European Research Council (ERC) under the European Union's Horizon Europe

research and innovation programme (grant agreement No. 101171380, project RUNES).

Author contributions

T.L.: Methodology, Software, Investigation, Visualization, Writing—Original draft preparation. G.P.: Conceptualization, Methodology, Investigation, Visualization, Writing—Original draft preparation. T.G.: Methodology, Validation, Writing- Original draft preparation. F.B.: Conceptualization, Methodology, Writing—Original draft preparation.

Declarations

Competing interests

The authors declare no competing interests.

Additional information

Supplementary Information The online version contains supplementary material available at https://doi.org/10.1038/s41598-025-04932-2.

Correspondence and requests for materials should be addressed to T.G.

Reprints and permissions information is available at www.nature.com/reprints.

Publisher's note Springer Nature remains neutral with regard to jurisdictional claims in published maps and institutional affiliations.